

# Evidence for a competition between the superconducting spin-valve effect and quasiparticle spin-decay in superconducting spin-valves

B. Stoddart-Stones,\* X. Montiel, M. G. Blamire, and J. W. A. Robinson†

*Department of Materials Science & Metallurgy, University of Cambridge,  
27 Charles Babbage Road, Cambridge CB3 0FS, United Kingdom*

(Dated: January 7, 2022)

The difference in the density of states for up- and down-spin electrons in a ferromagnet (F) results in spin-dependent scattering of electrons at a ferromagnet / nonmagnetic (F/N) interface. In a F/N/F spin-valve, this causes a current-independent difference in resistance ( $\Delta R$ ) between antiparallel (AP) and parallel (P) magnetization states. Giant magnetoresistance (GMR),  $\Delta R = R(AP) - R(P)$ , is positive due to increased scattering of majority and minority spin-electrons in the AP-state. If N is substituted for a superconductor (S), there exists a competition between GMR and the superconducting spin-valve effect: in the AP-state the net magnetic exchange field acting on S is lowered and the superconductivity is reinforced meaning  $R(AP)$  decreases. For current-perpendicular-to-plane (CPP) spin-valves, existing experimental studies show that GMR dominates ( $\Delta R > 0$ ) over the superconducting spin valve effect ( $\Delta R < 0$ ) [J. Y. Gu *et al.*, Phys. Rev. B 66, 140507(R) (2002)]. Here, however, we report a crossover from GMR ( $\Delta R > 0$ ) to the superconducting spin valve effect ( $\Delta R < 0$ ) in CPP F/S/F spin-valves as the superconductor thickness decreases below a critical value.

## I. INTRODUCTION

The field of spintronics [1] emerged following the discovery of spin-dependent scattering of electrons at ferromagnetic/nonmagnetic (F/N) interfaces [2] and giant magnetoresistance (GMR) in F/N/F structures [3]. In a F/N/F spin-valve, GMR is the difference in electrical resistance ( $\Delta R$ ) between antiparallel (AP) and parallel (P) magnetisation states of the F layers and is current-bias independent. In the AP-state, both the majority and minority spin-electrons are strongly scattered and  $\Delta R = R(AP) - R(P) > 0$  with the magnitude of  $\Delta R$  dependent on the spin-polarization of the F layers, interfacial spin-flip, and the spin decay length in N [4, 5].

In superconducting F/S/F spin-valves [6–8], the superconducting critical temperature ( $T_c$ ) depends on the magnetic moment orientation of the F layers due to the superconducting spin valve effect: in the P-state, the magnetic exchange fields suppress  $T_c(P)$  relative to  $T_c(AP)$  in which the magnetic exchange fields partially cancel meaning  $\Delta T_c = T_c^{AP} - T_c^P > 0$ . This effect allows the superconducting spin-valve to act as a valve for superconducting current flow, demonstrating infinite magnetoresistance, via switching the magnetic state of a device with suitably large  $\Delta T_c$  held at constant temperature. This current-bias independent behaviour is observed in current-in-plane (CIP) F/S/F spin-valves with  $\Delta T_c$  reaching tens of mK for transition metal Fs [9–18] and several hundred mK for rare-earth ferromagnetic metals and insulators [19–21]. These experimental values of  $\Delta T_c$  are orders of magnitude smaller than values predicted by theory [6–8], as it has proven experimentally challenging to reach the theoretically indicated op-

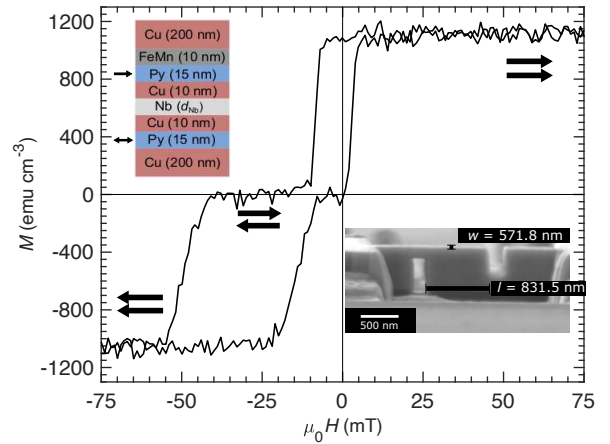


FIG. 1. Magnetization ( $M$ ) vs. in-plane magnetic field ( $H$ ) hysteresis loop for an unpatterned spin-valve at 10 K (arrows indicate the net magnetic moment directions of the top and bottom Py layers). Inset top left: Schematic diagram of the superconducting spin-valve. Arrows represent pinned (top) and free (bottom) ferromagnetic layers. Inset bottom right: Scanning electron micrograph of a nanopillar spin-valve. ‘Length’ ( $l = 831.5 \pm 40$  nm) and ‘width’ ( $w = 571.8 \pm 40$  nm) of the device are labelled. Device area,  $A = l \times w = 4.7 \pm 0.4 \times 10^5$  nm<sup>2</sup>.

timum parameter space. Negative  $\Delta T_c$  values have also been reported [14, 22–30], attributed either to quasiparticle (QP) spin-accumulation [23, 26, 28] suppressing  $T_c$  in the AP-state [31, 32], or flux penetration in S from out-of-plane domain walls in the F layers [14, 24, 27, 30].

Current-perpendicular-to-plane (CPP) devices have larger values of GMR than CIP devices [33–36], but are less investigated due to the extra complications of fabrication compared to CIP spin-valves, and so investigation into CPP devices with superconducting spin-valves has been limited. One reported CPP device [37] was a F/S/F

\* bs507@cam.ac.uk

† jjr33@cam.ac.uk

spin-valve, which showed GMR behaviour ( $\Delta R > 0$ ) due to quasiparticle transport (“QP GMR”) with a reduced spin decay length relative to the normal state for superconducting Nb layer thicknesses exceeding 30 nm. We note that the superconducting spin-valve effect ( $\Delta R < 0$ ) was not observed and that superconducting devices with thicknesses below 30 nm were not reported in [37].

In this article, we systematically investigate superconducting CPP F/S/F spin-valves with Py(15)/Cu(10)/Nb( $d_{\text{Nb}}$ )/Cu(10)/Py(15)/FeMn(10) layers (numbers in nm units) sandwiched between 200-nm-thick Cu electrodes (Fig. 1, inset top left). As expected, with decreasing Nb thickness ( $d_{\text{Nb}}$ ) QP GMR increases; however, below a critical thickness of superconducting Nb ( $d_{\text{Nb}} = 26$  nm) a sign change in  $\Delta R$  is observed, consistent with the appearance of the superconducting spin valve effect in these CPP devices, which dominates the QP GMR behaviour at these thicknesses. We show a systematic crossover between these competing behaviours, dependent on  $d_{\text{Nb}}$ .

## II. EXPERIMENTAL

The spin-valves are prepared by dc magnetron sputtering in an ultra-high vacuum chamber with a base pressure better than  $10^{-8}$  mbar. Films are deposited onto single crystal silicon with a 250-nm-thick surface oxide, with an in-plane magnetic field (100 mT) applied during growth to set in-plane uniaxial anisotropy. An antiferromagnetic layer of FeMn exchange biases the top layer of Py ( $\text{Ni}_{80}\text{Fe}_{20}$ ), ensuring a stable AP-state (Fig. 1). The Cu between the Nb and Py improves interface quality by limiting magnetic dead layers [38–40], and also increases the magnitude of magnetoresistance [37]. The spin-valves are patterned into nanopillars using optical lithography and Ga-ion focused ion-beam (FIB) etching (described elsewhere [41]). The lengths and widths of the nanopillars vary between 400-1500 nm and 300-1000 nm, respectively. Dimension and resistance values for each device are reported in Table S1 [42]. Resistance of the CPP spin-valves vs. temperature [ $R(T)$ ] or in-plane magnetic field [ $R(H)$ ] is measured using a ‘quasi’ four-point current-bias setup in a pulse-tube measurement system, which removes contact resistance. As Cu contact layers are used, the section under measurement is not exclusively the nanopillar device, but includes part of the patterned structure from which the nanopillar was milled, which is 4  $\mu\text{m}$  wide and 20  $\mu\text{m}$  long. This section of heterostructure, referred to as the ‘contact leads’, contributes to the measured resistance and so we refer to the measurement as ‘quasi’ four-point. Finally, in CPP measurements, since the cross-sectional areas ( $A$ ) of the CPP spin-valves vary,  $\Delta R$  is normalized by multiplying by  $A$  (i.e.  $A\Delta R$ ) [5]. Measurements were made on devices in both the normal state (above the superconducting transition of the nanopillar device and contact leads, but below 10 K) and in the superconducting state, although many devices

had such a suppressed transition temperature that they could not be measured in the S state. One important impact of the contact lead resistance is that  $R(T)$  measurements can appear to contain two distinct superconducting transitions [Fig. 2(a,d)]. The higher temperature transition (‘contact transition’) corresponds to the Nb in the contact leads, whereas the lower temperature transition (‘device transition’) corresponds to the nanopillar device. We define the onset temperature of the latter as  $T_{\text{device}}$ , and  $T_c$  as the temperature at 50% of the resistance change below  $T_{\text{device}}$  (Supplementary Material Section S-IIB [42]).

## III. RESULTS

$R(T)$  and  $R(H)$  measurements of two devices are shown in Fig. 2. Whilst the normal state  $R(H)$  loops [Fig. 2(b,e)] indicate GMR behaviour as expected, the superconducting state loops [Fig. 2(c,f)] reveal that two distinct behaviours appear in our devices, which is supported by the device transitions in Fig. 2(a,d); for the device with higher  $d_{\text{Nb}} = 28.5$  nm,  $T_c(AP) < T_c(P)$  and  $\Delta R > 0$ , consistent with the results in [37], suggesting GMR moderated by quasiparticles (QP GMR). For the device with lower  $d_{\text{Nb}} = 25$  nm  $\Delta R$  is negative [Fig. 2(c)], and  $T_c(P) < T_c(AP)$ . These results are those expected for superconducting spin-valve effect behaviour observed in CIP devices. The resistance increase with increasing field visible in Fig. 2(c) occurs for all superconducting spin-valve effect devices, which all have low  $H_{c2}$  values (being mid-transition at measurement temperatures), and therefore exhibit visible resistance increases within an applied magnetic field.

In Fig. 3 we show the absolute value  $A|\Delta R$  versus  $d_{\text{Nb}}$ , with data points and y-error representing the mean of multiple devices from a single substrate and their standard deviation respectively. Red data are from devices in their normal state (measured at  $< 10$  K) and blue data are from devices in the superconducting state at  $T/T_{\text{device}} = 0.3$ . Open circle data are devices demonstrating the superconducting spin valve effect. By fitting a simple decaying exponential,  $\exp(-d_{\text{Nb}}/l_{\text{sf}})$  [43], a reasonable approximation where the thickness of the ferromagnet (15 nm) is much greater than the spin-flip length in the ferromagnet (5.5 nm, [44]), we estimate spin-diffusion lengths from the GMR data in both the normal and superconducting states:  $l_{\text{sf}}^{\text{N}} = 25 \pm 3$  nm, and  $l_{\text{sf}}^{\text{S}} = 12 \pm 4$  nm. The decay length for QP GMR (in the superconducting state) is shorter than the normal state decay length, as found previously [37].

### A. Crossover

We now detail the main results of this article. To the best of our knowledge, the superconducting spin-valve effect has not been previously observed in CPP super-

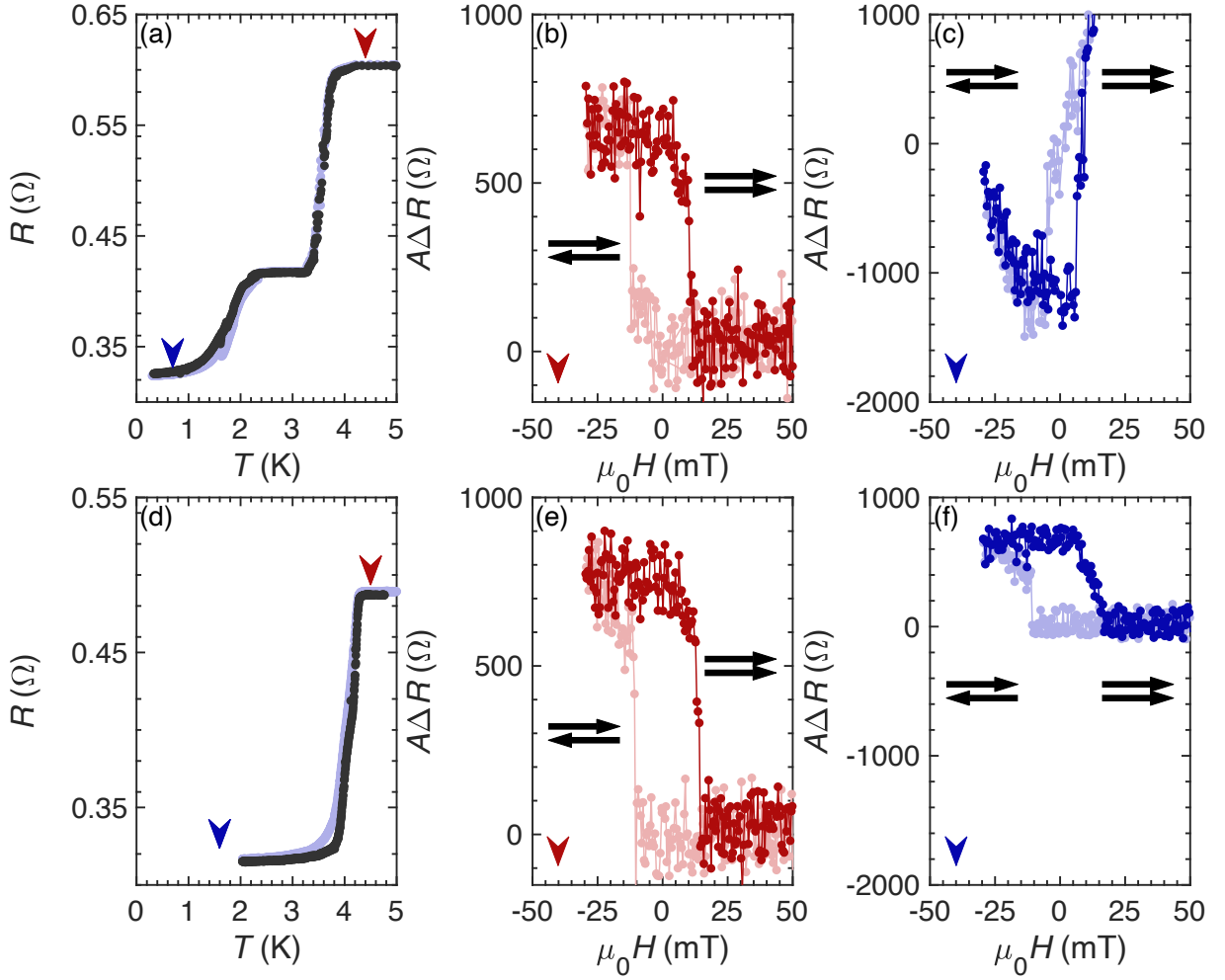


FIG. 2. The two different device responses observed. (a,d)  $R(T)$  curves for two different devices (top,  $d_{\text{Nb}} = 25$  nm; bottom,  $d_{\text{Nb}} = 28.5$  nm) in both the parallel (black) and antiparallel (blue) states. (b,e) Normal state minor  $R(H)$  loops from the same devices, both demonstrating GMR. (c,f) Minor  $R(H)$  loops in the superconducting state. The device with  $d_{\text{Nb}} = 25$  nm has greater resistance in the parallel state when superconducting, whereas the device with  $d_{\text{Nb}} = 28.5$  nm has greater resistance in the antiparallel state, similar to the normal state. For the  $R(H)$  loops, light data represent sweeps from positive to negative  $H$ , starting at high positive values. The dark data in each loop is for the return sweep. In these minor loops, only the free Py layer undergoes switching, illustrated by the black arrows, which show the relative magnetic moment orientation of the Py layers. Arrows in (a,d) indicate the temperature of the corresponding  $R(H)$  loops.

conducting spin valves, and so we investigate the factors that determine the appearance of this effect.

In Fig. 4 we plot  $A\Delta R$  at  $T/T_{\text{device}} = 0.3$  versus  $d_{\text{Nb}}$ , which shows a systematic dependence of  $A\Delta R$  on  $d_{\text{Nb}}$ , with a crossover from positive to negative  $A\Delta R$  occurring at  $d_{\text{Nb}} = 26$  nm. The inset shows the equivalent trend of  $\Delta T_c$  versus  $d_{\text{Nb}}$ . For  $d_{\text{Nb}} = 21$  nm, the superconducting spin valve effect reaches a positive  $\Delta T_c$  up to 299 mK [Fig. S1(a) [42]], which is unprecedented in transition metal F/S/F spin-valves where values are usually of the order tens of mK [9–18, 22–30]. However, we note that these large values of  $\Delta T_c$  are linked to inflation of  $A\Delta R$ ; devices showing the superconducting spin-valve effect have suppressed and broadened device transitions [transition width  $> 1$  K in Fig. 2(a)], meaning even these

large  $\Delta T_c$  values will not allow infinite magnetoresistance (complete switching between superconducting or normal states at a constant temperature). By considering the impact of superconductivity rather than just  $d_{\text{Nb}}$ , using  $T_{\text{device}}$  as the independent parameter, the outlier points at  $d_{\text{Nb}} = 31$  nm were shown to agree far better with the overall trend in the data [Fig. S2(a) [42]]. This led to consideration of the value  $d_{\text{Nb}}/\xi_{S,d}$ , where  $\xi_{S,d}$  is the dirty limit coherence length in the superconductor, calculated using

$$\xi_{S,d} = \sqrt{\frac{\hbar D}{1.764 k_B T_{\text{device}}}},$$

where  $D = 1.4 \times 10^{-4} \text{ m}^2 \text{ s}^{-1}$  is the electron diffusivity, calculated from a coherence length measurement of an

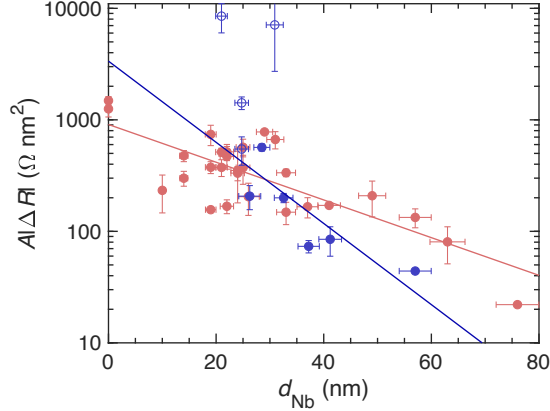


FIG. 3.  $A|\Delta R|$  vs.  $d_{\text{Nb}}$  in CPP spin valves for both the normal state (below 10 K, red) and superconducting state (blue). Closed blue circles are devices showing quasiparticle giant magnetoresistance, whereas open circles show the superconducting spin valve effect. Fits are to a simple exponential decay as described in the text, and open circle points are not included in the superconducting fit. Points are the mean value from multiple devices on a single substrate; vertical error bars are the standard deviation in  $A\Delta R$  of these devices and horizontal error bars the uncertainty in  $d_{\text{Nb}}$ .

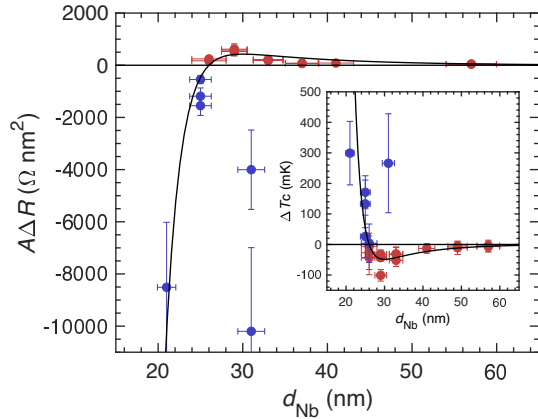


FIG. 4.  $A\Delta R$  at  $T/T_{\text{device}} = 0.3$  vs.  $d_{\text{Nb}}$ , with the inset  $\Delta T_c$  vs.  $d_{\text{Nb}}$ . Red points show QP GMR dominated behaviour, blue the superconducting spin valve effect dominated behaviour. Points represent individual spin-valve devices. Black curves are fits as described in the main text. The crossover point is  $d_{\text{Nb}} = 26$  nm.

isolated 30 nm Nb film, and  $k_B$  is Boltzmann's constant. Using this normalised  $d_{\text{Nb}}$ , we account for both thickness and processing effects which may affect the superconductivity in the devices. Figure 5 shows  $A\Delta R$  at  $T/T_{\text{device}} = 0.3$  and (Inset)  $\Delta T_c$  vs.  $d_{\text{Nb}}/\xi_{S,d}$ , which shows that the crossover between the two behaviours occurs at around  $d_{\text{Nb}} = 2\xi_{S,d}$ .

Both Fig. 4 and Fig. 5 show the same overall trend: with decreasing  $d_{\text{Nb}}$ , QP GMR (red) increases as ex-

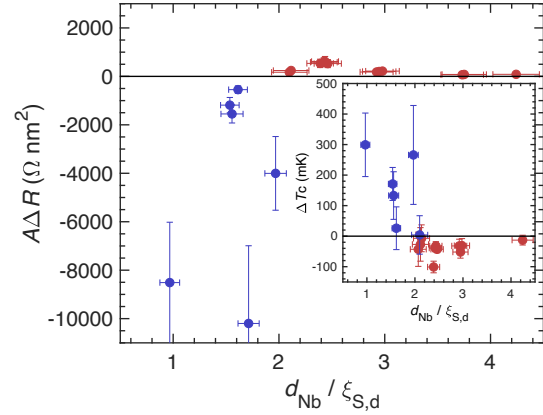


FIG. 5.  $A\Delta R$  at  $T/T_{\text{device}} = 0.3$  vs.  $d_{\text{Nb}}/\xi_{S,d}$ , with inset  $\Delta T_c$  vs.  $d_{\text{Nb}}/\xi_{S,d}$ . Red points show QP GMR dominated behaviour, blue the superconducting spin valve effect dominated behaviour. Points represent individual spin-valve devices. The crossover point between the two behaviours occurs around  $d_{\text{Nb}} = 2\xi_{S,d}$ .

pected, but then peaks and decreases rapidly, devices crossing over into superconducting spin-valve effect dominated behaviour, which rapidly increases in magnitude with decreasing  $d_{\text{Nb}}$ . The ‘peak then fall’ shape of the trend indicates that rather than being a sudden switch from QP GMR to superconducting spin-valve effect behaviour, these are two separate effects which compete within the devices.

The crossover between positive and negative values of  $A\Delta R$  is clear and the magnitude is significant, ruling out minor background effects. Scatter of the data does not account for the crossover behaviour, as indicated by a plot of  $\Delta R$  at  $T/T_{\text{device}} = 0.3$  normalised by  $\Delta R$  in the normal state [Fig. S2(b) [42]].

#### IV. DISCUSSION

The ‘double’ transition visible within these devices highlights the contribution of the ‘contact leads’ to the measured resistance in these devices. It also highlights that the lower transition - the device transition - tends to be more suppressed in devices demonstrating the superconducting spin-valve effect compared to those demonstrating QP GMR [compare Fig. 2(a) and (d), which feature device transitions around 2 K apart, whereas the ‘contact’ transitions differ by less than 1 K]. This observation suggests not only  $d_{\text{Nb}}$ , but also the strength of superconducting order within the devices affect the appearance of the superconducting spin-valve effect.

Below their superconducting transition, the contact leads are superconducting and do not contribute to the measured  $R(H)$  response, as shown in the inset to Fig. 6(a), which was measured on the contact leads only. The exception to this is the substrate with thinnest



$d_{\text{Nb}} = 21$  nm: even at the lowest temperatures, the contact leads demonstrate an  $R(H)$  response which also shows the superconducting spin valve effect [Fig. 6(a)], which may contribute to the large magnitude of the measured effect for that device.

We have considered alternative explanations for the negative  $\Delta R$  in our devices [Fig 2(e)] including anisotropic magnetoresistance [45]. However, this is ruled out since anisotropic magnetoresistance is not observed in these superconducting spin-valve effect devices above  $T_c$  [Fig. 2(b)]. Additionally, the zero field  $R(T)$  measurements show distinct differences between P- and AP-states and anisotropic magnetoresistance would not lead to such differences in the absence of an applied magnetic field [3]. Negative magnetoresistance could also result from crossed Andreev reflection (CAR) [46–50] of electrons across the superconducting layer, when the layer is less than one superconducting coherence length thick. CAR has previously been considered as a source of magnetoresistance in CIP spin valves [51], but is generally considered as a non-local effect. We note that there is one report of CAR measured in a local setup [52], but the origin of magnetoresistance in this case is uncertain.

The values for spin decay length calculated in our devices ( $l_{\text{sf}}^{\text{N}} = 25 \pm 3$  nm, and  $l_{\text{sf}}^{\text{S}} = 12 \pm 4$  nm) can be compared with other values from the literature. A similar CPP structure has been used previously [37] to measure values of  $l_{\text{sf}}^{\text{N}} = 48 \pm 3$  nm and  $l_{\text{sf}}^{\text{S}} = 17.5 \pm 0.6$  nm. Additionally, a value of  $l_{\text{sf}}^{\text{N}} = 40 \pm 5$  nm was extracted from a fit to ferromagnetic resonance data [53]. These literature values are larger than the values measured here; we attribute this difference to increased scattering due to impurities and defects introduced during the nanopatterning process. These defects may also contribute to the separation of device and ‘contact lead’ superconducting transitions. This separation is inconsistent even between devices on the same substrate, as demonstrated in Fig. 6(b), which we cannot currently explain. If FIB milling were accountable for this transition separation, the separation would scale with nanopillar area. However, as shown in the inset to Fig. 6(b), the transition temperature of the device transition, represented by the starting temperature  $T_{\text{device}}$ , does not demonstrate any dependence on device area. This uncertainty around the double transition does not affect the main observation of this paper; the appearance of the superconducting spin valve effect in both  $R(H)$  and  $R(T)$  measurements and a thickness dependent crossover between them.

The comparison of positive magnetoresistance data above and below  $T_c$  supports the suggestion that CPP devices demonstrate QP GMR, as originally demonstrated in [37]. Like in that paper, we also observe a decrease in spin decay length in the superconducting state which is consistent with the additional impact of Andreev reflection causing decay of quasiparticles that cause this magnetoresistance. Unlike [37], we have also measured superconducting devices with  $d_{\text{Nb}}$  smaller than the thickness at which Andreev reflection does not appear to play

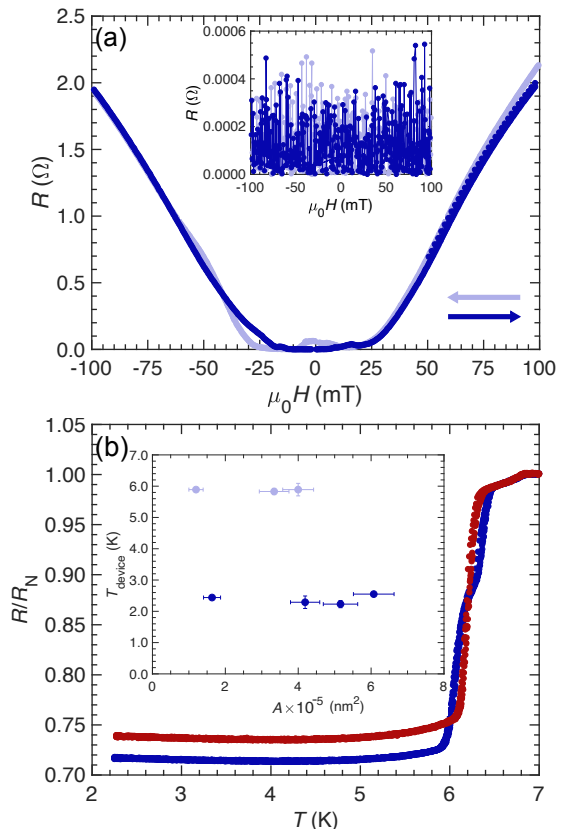


FIG. 6. (a) Major  $R(H)$  loop measured on the contact leads at 0.3 K for the device with  $d_{\text{Nb}} = 21$  nm. For this device only, there is a magnetoresistance response in the contact leads at the measurement temperature, which is negative (parallel state is higher resistance). In all other devices, the leads are superconducting below the contact lead transition, and show no magnetoresistance response at  $T/T_{\text{device}} = 0.3$ , as shown in the Inset. (b)  $R(T)$  curves from two devices on the same substrate, normalised by their normal state resistance for comparison. The separate Nb in the nanopillar devices and the contact leads is the origin of the ‘double transition’ visible in  $R(T)$  curves. The difference between the temperature of each transition varies in an unknown manner, and can be small enough that the double transition is not distinguishable. Inset:  $T_{\text{device}}$  vs. nanopillar area, for a device showing the superconducting spin valve effect ( $d_{\text{Nb}} = 25$  nm, dark blue) and a device showing QP GMR ( $d_{\text{Nb}} = 37$  nm, light blue). There is no dependence of  $T_{\text{device}}$  on area, which may have been expected due to nanopatterning.

a role. These devices are those that demonstrate the superconducting spin-valve effect, having negative  $A\Delta R$ . The crossover between these two effects appears to occur at around  $d_{\text{Nb}} = 26$  nm, which is close to twice  $l_{\text{sf}}^{\text{S}} = 12 \pm 4$  nm, similar to [37], and further supported by Fig. 5, which suggests the crossover occurs where  $d_{\text{Nb}} = 2\xi_{\text{S,d}}$ .

### A. Phenomenological model

A model in [37] assumes QP GMR in CPP F/S/F spin-valves decays due to Andreev reflection as quasiparticles pass a potential barrier with a temperature-dependent height i.e.  $\Delta^{AP} = \Delta^P = \Delta(T)$ , and reduced thickness  $d_{\text{Nb}} - d_0$ , where  $d_0/2$  is the thickness of the region near each F/S interface where the superconducting gap and Andreev reflection are suppressed, expected to be equal to the coherence length. This approximation captures the QP GMR results in Fig. 4 beyond  $d_{\text{Nb}} = 26$  nm, but cannot describe our superconducting spin-valve effect data.

We extend these ideas from [37], in a toy model that simply illustrates the two competing effects within our devices, capturing the overall trend as the difference of two exponential decays

$$\Delta R = A \exp\left[\frac{-(d_{\text{Nb}} - d_0)}{l_S}\right] - B \exp\left[\frac{-(d_{\text{Nb}} - d_0)}{\Lambda_S}\right],$$

where the first term relates to QP GMR ( $\Delta R > 0$ ), as in the model from [37] and the second to the superconducting spin valve effect ( $\Delta R < 0$ ), with a characteristic decay  $\Lambda_S$ . We choose an exponential for this decay to reproduce the distinct shape of the data in Fig. 4. In this thinner Nb regime,  $T_c(AP) > T_c(P)$  meaning that the superconducting spin-valve effect enhances  $\Delta^{AP}$  [7, 8]; leading to decreased resistance as a greater proportion of the Nb is superconducting. We set  $d_0 = 26$  nm, the crossover thickness, causing  $|A/B| = 1$ , and set  $l_S$  to the value  $l_{\text{sf}}^S = 12 \pm 4$ . We find a value for  $\Lambda_S = 2.2 \pm 0.7$  nm as an average and deviation from orthogonal distance regression on the  $A\Delta R$  and  $\Delta T_c$  data, which fits both data sets. This value is very small and does not initially appear to represent a physical length; however, we note previous superconducting spin-valve investigations [11] have seen a dramatic shift from a  $\Delta T_c$  of 41 mK to “only a few mK” for an increase in  $d_{\text{Nb}}$  of only 1 nm, which could only be modelled by theory using parameters that did not match the estimates of the authors. These short de-

clays lengths may reflect some experimental effects not accounted for by theory based fits. Overall, this toy model illustrates coexistence of the superconducting spin-valve effect and QP GMR, which are competing effects within these devices.

Previous studies showing both positive and negative values of  $\Delta R$  are explained on the basis of stray magnetic fields or vortex flow from a multi-domain state of one or both coupled F layers [14, 29, 54]. In our spin-valves positive  $\Delta R$  is expected due to QP GMR, and a multidomain state with out-of-plane stray magnetic fields would cause positive magnetoresistance within the transition region, which is far from the measurement temperature of our QP GMR data [Fig. 2(b)]. No studies that we are aware of have demonstrated a systematic change of sign of magnetoresistance with  $d_{\text{Nb}}$ , such as the crossover we show here.

### V. CONCLUSION

In summary, we have presented evidence for a competition between QP GMR and the superconducting spin valve effect in superconducting CPP spin-valves. Below a Nb thickness of  $d_{\text{Nb}} \approx 26$  nm,  $\Delta R$  is negative and determined by the superconducting spin valve effect; beyond this critical thickness,  $\Delta R$  is positive with a magnitude that is determined by QP Andreev reflection. This thickness appears to correspond to twice the dirty limit coherence length of the devices. These results are relevant to development of quasiparticle spintronics devices, suggesting devices utilising QP GMR effects should be fabricated with  $d_{\text{Nb}} > 26$  nm, or consider using the superconducting spin valve effect.

### ACKNOWLEDGMENTS

This work was funded by the EPSRC through a DTP Studentship (nos. EP/M508007/1 and EP/N509620/1) and Programme Grant (no. EP/N017242/1).

- 
- [1] I. Žutić, J. Fabian, and S. Das Sarma, *Rev. Mod. Phys.* **76**, 323 (2004).
  - [2] M. Johnson and R. H. Silsbee, *Phys. Rev. Lett.* **55**, 1790 (1985).
  - [3] B. Dieny, V. S. Speriosu, S. S. P. Parkin, B. A. Gurney, D. R. Wilhoit, and D. Mauri, *Phys. Rev. B* **43**, 1297 (1991).
  - [4] T. Valet and A. Fert, *J. Magn. Magn. Mater.* **121**, 378 (1993).
  - [5] J. Bass, *J. Magn. Magn. Mater.* **408**, 244 (2016).
  - [6] S. Oh, D. Youm, and M. R. Beasley, *Appl. Phys. Lett.* **71**, 2376 (1997).
  - [7] L. R. Tagirov, *Phys. Rev. Lett.* **83**, 2058 (1999).
  - [8] A. Buzdin and A. Vedyayev, *Europhysics Lett.* **48**, 686 (1999).
  - [9] J. Y. Gu, C.-Y. You, J. S. Jiang, J. Pearson, Y. B. Bazaliy, and S. D. Bader, *Phys. Rev. Lett.* **89**, 267001 (2002).
  - [10] A. Potenza and C. H. Marrows, *Phys. Rev. B* **71**, 180503(R) (2005).
  - [11] I. C. Moraru, W. P. Pratt, and N. O. Birge, *Phys. Rev. Lett.* **96**, 037004 (2006).
  - [12] I. C. Moraru, W. P. Pratt, and N. O. Birge, *Phys. Rev. B* **74**, 220507(R) (2006).
  - [13] G.-X. Miao, A. V. Ramos, and J. S. Moodera, *Phys. Rev. Lett.* **101**, 137001 (2008).
  - [14] J. Zhu, X. Cheng, C. Boone, and I. N. Krivorotov, *Phys. Rev. Lett.* **103**, 027004 (2009).
  - [15] P. V. Leksin, N. N. Garif'yanov, I. A. Garifullin, J. Schumann, H. Vinzelberg, V. Kataev, R. Klingeler, O. G. Schmidt, and B. Büchner,

- Appl. Phys. Lett.* **97**, 102505 (2010).
- [16] J. Zhu, I. N. Krivorotov, K. Halterman, and O. T. Valls, *Phys. Rev. Lett.* **105**, 207002 (2010).
- [17] P. V. Leksin, N. N. Garif'yanov, A. A. Kamashev, Y. V. Fominov, J. Schumann, C. Hess, V. Kataev, B. Büchner, and I. a. Garifullin, *Phys. Rev. B* **91**, 214508 (2015).
- [18] A. A. Jara, E. Moen, O. T. Valls, and I. N. Krivorotov, *Phys. Rev. B* **100**, 184512 (2019).
- [19] Y. Gu, G. B. Halász, J. W. A. Robinson, and M. G. Blamire, *Phys. Rev. Lett.* **115**, 067201 (2015).
- [20] B. Li, N. Roschewsky, B. A. Assaf, M. Eich, M. Epstein-Martin, D. Heiman, M. Münzenberg, and J. S. Moodera, *Phys. Rev. Lett.* **110**, 097001 (2013).
- [21] Y. Zhu, A. Pal, M. G. Blamire, and Z. H. Barber, *Nat. Mater.* **1**, 1 (2016).
- [22] J. Aarts and A. Y. Rusanov, *Comptes Rendus Phys.* **7**, 99 (2006).
- [23] A. Y. Rusanov, S. Habraken, and J. Aarts, *Phys. Rev. B* **73**, 060505(R) (2006).
- [24] R. Steiner and P. Ziemann, *Phys. Rev. B* **74**, 094504 (2006).
- [25] A. Singh, C. Sürgers, and H. v. Löhneysen, *Phys. Rev. B* **75**, 024513 (2007).
- [26] A. Singh, C. Sürgers, R. Hoffmann, H. V. Löhneysen, T. V. Ashworth, N. Pilet, and H. J. Hug, *Appl. Phys. Lett.* **91**, 71 (2007).
- [27] D. Stamopoulos, E. Manios, and M. Pissas, *Phys. Rev. B* **75**, 184504 (2007).
- [28] P. V. Leksin, R. I. Salikhov, I. A. Garifullin, H. Vinzelberg, V. Kataev, R. Klingeler, L. R. Tagirov, and B. Büchner, *JETP Lett.* **90**, 59 (2009).
- [29] T. J. Hwang, D. H. Kim, and S. Oh, *IEEE Trans. Magn.* **46**, 235 (2010).
- [30] M. Flokstra, J. M. van der Knaap, and J. Aarts, *Phys. Rev. B* **82**, 184523 (2010).
- [31] S. Takahashi, H. Imamura, and S. Maekawa, *Phys. Rev. Lett.* **82**, 3911 (1999).
- [32] S. Takahashi and S. Maekawa, *Phys. Rev. B* **67**, 052409 (2003).
- [33] W. P. Pratt, S. F. Lee, J. M. Slaughter, R. Loloee, P. A. Schroeder, and J. Bass, *Phys. Rev. Lett.* **66**, 3060 (1991).
- [34] S. F. Lee, Q. Yang, P. Holody, R. Loloee, J. H. Hetherington, S. Mahmood, B. Ikegami, K. Vigen, L. L. Henry, P. A. Schroeder, W. P. Pratt, and J. Bass, *Phys. Rev. B* **52**, 15426 (1995).
- [35] M. A. Gijs, S. K. Lenczowski, J. B. Giesbers, R. J. van de Veerdonk, M. T. Johnson, and J. B. aan de Stegge, *Mater. Sci. Eng. B* **31**, 85 (1995).
- [36] K. Eid, D. Portner, J. A. Borchers, R. Loloee, M. Al-Haj Darwish, M. Tsoi, R. D. Slater, K. V. O'Donovan, H. Kurt, W. P. Pratt, and J. Bass, *Phys. Rev. B* **65**, 544241 (2002).
- [37] J. Y. Gu, J. A. Caballero, R. D. Slater, R. Loloee, and W. P. Pratt, *Phys. Rev. B* **66**, 140507(R) (2002).
- [38] C. Bell, R. Loloee, G. Burnell, and M. G. Blamire, *Phys. Rev. B* **71**, 180501(R) (2005).
- [39] J. W. A. Robinson, S. Piano, G. Burnell, C. Bell, and M. G. Blamire, *Phys. Rev. B* **76**, 094522 (2007).
- [40] G. Tateishi and G. Bergmann, *Eur. Phys. J. B* **73**, 155 (2010).
- [41] C. Bell, G. Burnell, D.-J. Kang, R. H. Hadfield, M. J. Kappers, and M. G. Blamire, *Nanotechnology* **14**, 630 (2003).
- [42] See Supplemental Material at [URL will be inserted by publisher] for (I) data and additional figures, (II) the wires leading to the device and (III) fitting details for above and below  $T_c$  fits.
- [43] W. Park, D. V. Baxter, S. Steenwyk, I. Moraru, W. P. Pratt, and J. Bass, *Phys. Rev. B* **62**, 1178 (2000).
- [44] L. Vila, W. Park, J. A. Caballero, D. Bozec, R. Loloee, W. P. Pratt, and J. Bass, *J. Appl. Phys.* **87**, 8610 (2000).
- [45] T. R. Mcguire and R. I. Potter, *IEEE Trans. Magn.* **11**, 1018 (1975).
- [46] G. Deutscher and D. Feinberg, *Appl. Phys. Lett.* **76**, 487 (2000).
- [47] D. Beckmann, E. B. Weber, and H. V. Löhneysen, *Phys. Rev. Lett.* **93**, 197003 (2004).
- [48] D. Beckmann and H. V. Löhneysen, *Appl. Phys. A Mater. Sci. Process.* **89**, 603 (2007).
- [49] A. Kleine, A. Baumgartner, J. Trbovic, and C. Schönenberger, *Europhys. Lett.* **87**, 10.1209/0295-5075/87/27011 (2009).
- [50] J. L. Webb, B. J. Hickey, and G. Burnell, *Phys. Rev. B* **86**, 054525 (2012).
- [51] F. Giazotto, F. Taddei, F. Beltram, and R. Fazio, *Phys. Rev. Lett.* **97**, 087001 (2006).
- [52] P. Cadden-Zimansky, Z. Jiang, and V. Chandrasekhar, *New J. Phys.* **9**, 10.1088/1367-2630/9/5/116 (2007).
- [53] K.-R. Jeon, C. Ciccarelli, A. J. Ferguson, H. Kurebayashi, L. F. Cohen, X. Montiel, M. Eschrig, J. W. A. Robinson, and M. G. Blamire, *Nat. Mater.* **17**, 499 (2018).
- [54] T. J. Hwang and D. H. Kim, *J. Korean Phys. Soc.* **61**, 1628 (2012).

**Evidence for competition between the superconductor proximity  
effect and quasiparticle spin-decay in superconducting spin-valves:**

**Supplemental Material**

B. Stoddart-Stones,<sup>\*</sup> X. Montiel, M. G. Blamire, and J. W. A. Robinson<sup>†</sup>

5

*Department of Materials Science & Metallurgy,  
University of Cambridge, 27 Charles Babbage Road,  
Cambridge CB3 0FS, United Kingdom*

(Dated: January 7, 2022)



## S-I. DATA AND FIGURES

$d_{\text{Nb}}$ (nm)	Pillar length (nm)	Pillar width (nm)	$R_{\text{N}}^{\text{AP}}$ ( $\Omega$ )	$R_{\text{N}}^{\text{P}}$ ( $\Omega$ )	$R_{\text{S}}^{\text{AP}}$ ( $\Omega$ )	$R_{\text{S}}^{\text{P}}$ ( $\Omega$ )
0	665	547	0.3143	0.3110		
0	842	865	0.2075	0.2060		
0	815	900	0.2285	0.2265		
24	447	509	0.2378	0.2372		
24	551	455	0.4469	0.4459		
24	703	489	0.4374	0.4362		
24	848	491	0.4004	0.3995		
24	946	464	0.5198	0.5184		
14	825	525	0.6227	0.6221		
14	841	606	0.4799	0.4792		
14	1020	651	0.5218	0.5214		
33	811	388	0.6146	0.6143		
33	673	370	0.7469	0.7462		
33	1280	784	0.6708	0.6707		
33	1020	737	0.4965	0.4963		
33	910	658	0.5152	0.5150		
19	437	596	0.8595	0.8589		
14	886	611	0.6072	0.6063		
14	1088	551	0.6381	0.6374		
24	1111	478	0.5056	0.5051		
24	1322	581	0.3868	0.3864		
24	892	423	0.5230	0.5221		
24	1318	617	0.3780	0.3775		
22	722	541	0.5423	0.5418		
22	725	539	0.6677	0.6673		

*Continued on next page*

---

\* [bs507@cam.ac.uk](mailto:bs507@cam.ac.uk)

† [jjr33@cam.ac.uk](mailto:jjr33@cam.ac.uk)

TABLE S1 – *Continued from previous page*

$d_{\text{Nb}}$ (nm)	Pillar length (nm)	Pillar width (nm)	$R_{\text{N}}^{\text{AP}}$ ( $\Omega$ )	$R_{\text{N}}^{\text{P}}$ ( $\Omega$ )	$R_{\text{S}}^{\text{AP}}$ ( $\Omega$ )	$R_{\text{S}}^{\text{P}}$ ( $\Omega$ )
22	720	527	0.5465	0.5461		
22	749	693	0.5936	0.5924		
22	736	615	0.7919	0.7910		
22	712	479	0.7673	0.7660		
22	679	416	1.1350	1.1335		
25	350	468	0.7364	0.7334		
25	522	457	0.7112	0.7090		
25	883	474	0.6783	0.6768	0.3242	0.3279
25	1078	479	0.5995	0.5984	0.3030	0.3055
25	1315	462	0.6682	0.6670		
25	1453	468	0.5252	0.5245		
19	805	492	0.5450	0.5429		
19	798	515	0.5140	0.5120		
19	791	500	0.5955	0.5935		
19	793	498	0.5319	0.5299		
19	791	494	0.5364	0.5353		
19	797	494	0.5378	0.5358		
21	927	501	0.4155	0.4147		
21	933	489	0.4376	0.4369		
21	940	529	0.3983	0.3975		
21	962	532	0.2836	0.2830		
21	937	538	0.4597	0.4588		
29	775	494	0.4893	0.4873	0.3083	0.3069
29	795	482	0.4931	0.4910		
29	779	499	0.5068	0.5048		
29	795	525	0.4930	0.4911	0.2995	0.2981
29	750	503	0.4978	0.4958	0.3472	0.3458

*Continued on next page*

TABLE S1 – *Continued from previous page*

$d_{\text{Nb}}$ (nm)	Pillar length (nm)	Pillar width (nm)	$R_{\text{N}}^{\text{AP}}$ ( $\Omega$ )	$R_{\text{N}}^{\text{P}}$ ( $\Omega$ )	$R_{\text{S}}^{\text{AP}}$ ( $\Omega$ )	$R_{\text{S}}^{\text{P}}$ ( $\Omega$ )
29	826	497	0.4676	0.4657	0.3149	0.3134
31	801	501	0.4476	0.4460		
31	821	521	0.4172	0.4155		
31	815	494	0.4592	0.4574		
31	792	501	0.5000	0.4982	0.2809	0.3066
31	799	490	0.4723	0.4713		
31	810	494	0.4211	0.4193		
31	812	525	0.4067	0.4050	0.1984	0.2078
21	749	623	0.4538	0.4528		
21	744	601	0.4754	0.4743		
21	736	595	0.4950	0.4938		
21	743	608	0.5490	0.5478		
21	710	564	0.5692	0.5680		
21	716	561	0.5308	0.5295		
21	714	590	0.5374	0.5360	0.3595	0.3797
57	721	639	0.4176	0.4173		
57	701	618	0.3803	0.3800	0.2560	0.2560
26	705	487	0.7084	0.7076		
26	696	488	0.7254	0.7246		
26	717	477	0.6197	0.6190	0.4819	0.4814
26	628	481	1.2160	1.2157		
26	699	467	0.7153	0.7148		
26	720	474	0.6588	0.6581	0.4746	0.4738
22	859	443	0.5679	0.5664		
22	828	463	0.5043	0.5028		
22	863	424	0.4914	0.4901		
22	817	470	0.4345	0.4330		

*Continued on next page*

TABLE S1 – *Continued from previous page*

$d_{\text{Nb}}$ (nm)	Pillar length (nm)	Pillar width (nm)	$R_{\text{N}}^{\text{AP}}$ ( $\Omega$ )	$R_{\text{N}}^{\text{P}}$ ( $\Omega$ )	$R_{\text{S}}^{\text{AP}}$ ( $\Omega$ )	$R_{\text{S}}^{\text{P}}$ ( $\Omega$ )
22	809	475	0.3262	0.3252		
63	697	495	0.3884	0.3881		
63	669	468	0.5185	0.5184		
63	670	505	0.4041	0.4038		
33	684	493	0.5600	0.5590		
33	716	504	0.5506	0.5497	0.3744	0.3739
33	705	516	0.5714	0.5705	0.4028	0.4022
33	676	481	0.6019	0.6008		
33	703	514	0.5554	0.5544		
33	689	487	0.5927	0.5917		
33	660	508	0.5345	0.5336	0.3492	0.3486
37	955	350	0.4722	0.4717	0.3784	0.3782
37	977	409	0.3531	0.3526	0.2817	0.2815
37	352	340	0.8040	0.8029		
41	915	314	0.4918	0.4912		
41	904	313	0.5724	0.5718	0.4944	0.4941
49	997	523	0.3201	0.3196		
49	578	541	0.2953	0.2948		
25	855	432	0.5645	0.5637	0.2570	0.2585
25	726	442	0.4891	0.4877		
19	970	729	0.3274	0.3268		
19	971	568	0.5102	0.5095		
19	957	564	0.5504	0.5498		
19	973	748	0.3149	0.3144		
19	962	532	0.4370	0.4364		
76	354	207	1.5758	1.5755		
10	497	576	0.3940	0.3931		

*Continued on next page*

TABLE S1 – *Continued from previous page*

$d_{\text{Nb}}$ (nm)	Pillar length (nm)	Pillar width (nm)	$R_{\text{N}}^{\text{AP}}$ ( $\Omega$ )	$R_{\text{N}}^{\text{P}}$ ( $\Omega$ )	$R_{\text{S}}^{\text{AP}}$ ( $\Omega$ )	$R_{\text{S}}^{\text{P}}$ ( $\Omega$ )
10	436	335	0.6459	0.6451		
10	528	567	0.3448	0.3442		
10	510	573	0.3593	0.3582		
10	640	564	0.3250	0.3245		
10	418	366	0.6174	0.6152		
0	452	759	0.2526	0.2480		
0	512	462	0.4457	0.4398		

TABLE S1: Table of raw data for the devices that appear in the graphs in the main paper and this Supplemental Material. Note that these resistance values include the contribution of the ‘contact leads’ next to the devices. All resistance values are at zero applied field. There are far fewer results in the superconducting state than normal state because many devices, especially for lower  $d_{\text{Nb}}$  values, did not go fully superconducting.

## 10 A. Further plots

Figure S1 is as Fig. 2 in the main paper, showing  $R(T)$  and  $R(H)$  loops for two more devices, which represent extremes of the two different behaviours observed in these papers. The top graphs come from the device with  $d_{\text{Nb}} = 21$  nm, which is the thinnest  $d_{\text{Nb}}$  tested. This device demonstrates superconducting spin valve effect behaviour even in the wires, 15 visible in Fig. S1(a), as the  $T_{\text{c}}$  of the parallel state is lower than that of the antiparallel state in the steep wires region. The device transition is noticeably extremely wide. The bottom graphs come from a device with  $d_{\text{Nb}} = 57$  nm, which is large, as reflected in the small values of  $A\Delta R$  in the  $R(H)$  loops and the negligible  $\Delta T_{\text{c}}$  in Fig. S1(d).

Figure S2(a) shows  $A\Delta R$  at  $T/T_{\text{device}} = 0.3$  and  $\Delta T_{\text{c}}$  as in the main text, but plotted 20 against  $T_{\text{device}}$ . The outlier points at -11,000 and -4,000  $\Omega \text{nm}^2$  agree with the main trend much better when this is used as the independent parameter, which suggests that the prop-



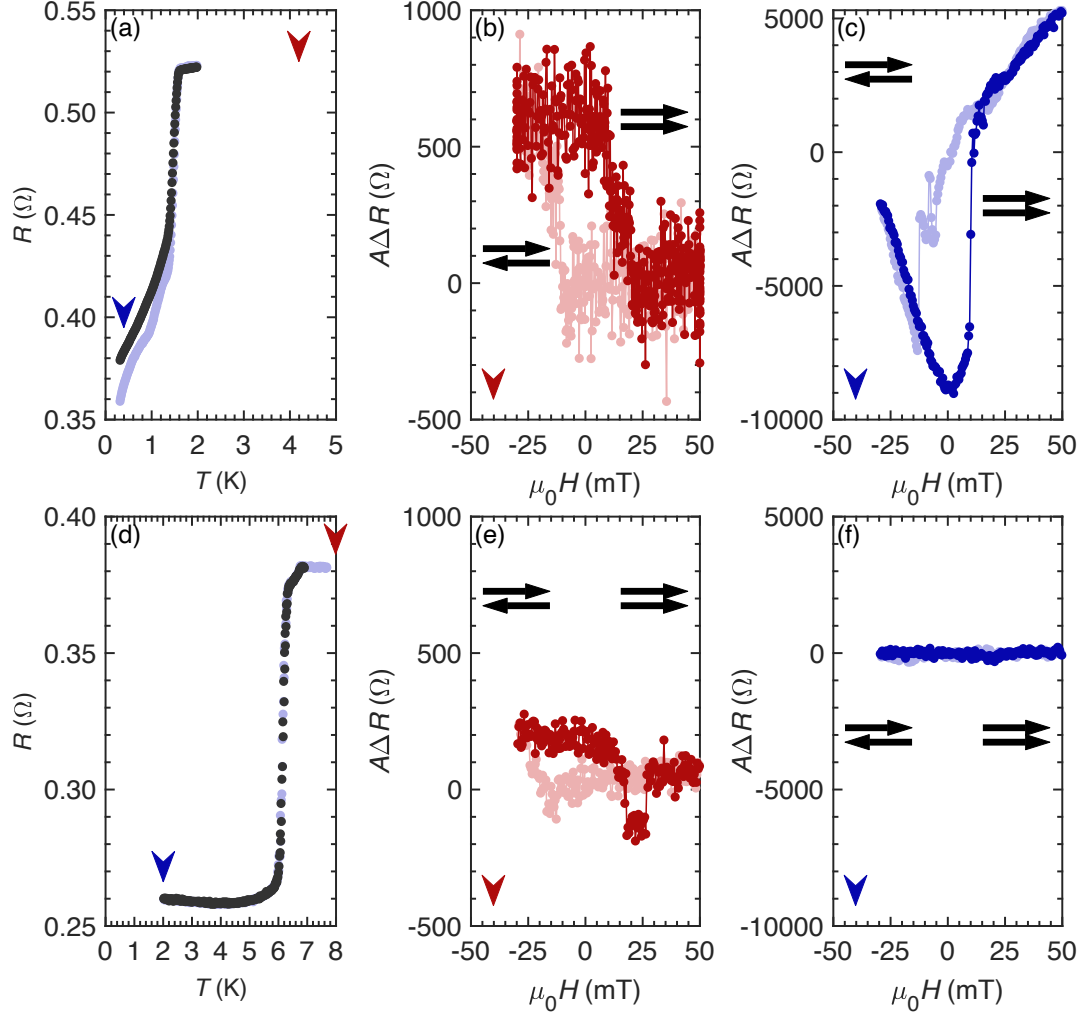


FIG. S1. (a,d)  $R(T)$  curves for two different devices (top,  $d_{\text{Nb}} = 21$  nm; bottom,  $d_{\text{Nb}} = 57$  nm) in both the parallel (black) and antiparallel (blue) states. (b,e) Normal state minor  $R(H)$  loops from the same devices, both demonstrating GMR. (c,f) Minor  $R(H)$  loops in the superconducting state. For the  $R(H)$  loops, light data represent sweeps from positive to negative  $H$ , starting at high positive values. The dark data in each loop is for the return sweep. In these minor loops, only the free Py layer undergoes switching, illustrated by the black arrows, which show the relative magnetic moment orientation of the Py layers. Arrows in (a,d) indicate the temperature of the corresponding  $R(H)$  loops.

erties of the superconductor, not just the spacing between the ferromagnets, influence the crossover behaviour. Figure S2(b) shows normalised data,  $\Delta R_S/\Delta R_N$  where  $\Delta R_S$  is  $\Delta R$  at  $T/T_{\text{device}} = 0.3$ , and  $\Delta R_N$  is  $\Delta R$  in the normal state, along with  $\Delta T_c/T_{\text{device}}$  in the inset.

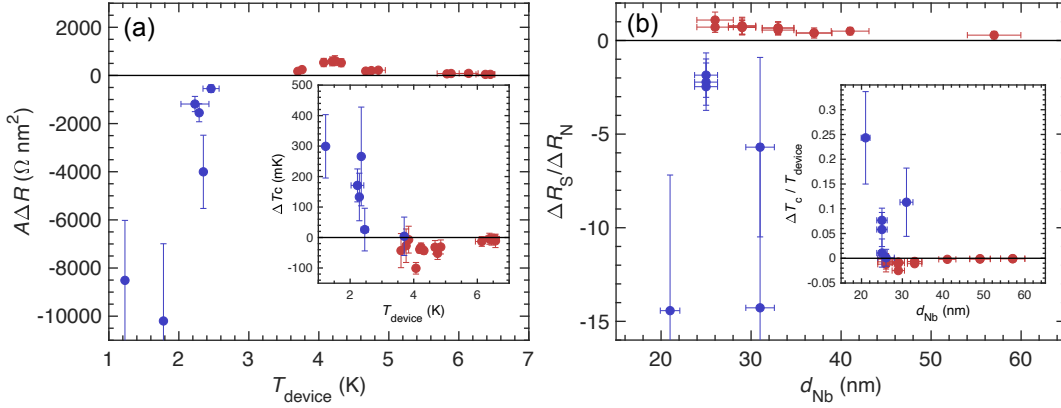


FIG. S2. (a)  $A\Delta R$  ( $T/T_{\text{device}} = 0.3$ ) and inset  $\Delta T_c$  vs.  $T_{\text{device}}$ . The crossover is still present, and points that were outliers when plotted vs.  $d_{\text{Nb}}$  now fit the trend better. (b)  $\Delta R$  at  $T/T_{\text{device}} = 0.3$  normalised by  $\Delta R$  in the normal state. Inset:  $\Delta T_c$  normalised by  $T_{\text{device}}$ .

25 The normalised data also show a sign change dependent on  $d_{\text{Nb}}$ , and the crossover occurs at a similar value of  $d_{\text{Nb}}$  to the standard data. This indicates the scatter shown by the devices is not responsible for the crossover and trend we see below  $T_c$ .

## S-II. DATA ANALYSIS

### A. Link between $\Delta R$ and $\Delta T_c$

30 Real (non-ideal) devices have a superconducting transition with a finite gradient, which leads to a link between  $\Delta R$  and  $\Delta T_c$  within this region, where the measurement of  $\Delta T_c$  occurs. Hence, as shown in Fig. S3, effects causing a shift in either  $\Delta R$  or  $\Delta T_c$  can cause a shift in the other parameter as well. This must be accounted for when considering devices with both the superconducting spin valve effect, which affects  $\Delta T_c$ , and GMR, which affects  
 35  $\Delta R$ .

### B. $\Delta T_c$ extraction

$\Delta T_c$  values were extracted from separate  $R(T)$  measurements of the parallel and antiparallel states of the devices, at  $R(T_c) = 0.5R_N^{AP}$ , where  $R_N^{AP}$  is the resistance at  $T_{\text{device}}$ , the onset of the device transition in the antiparallel state. A single  $0.5R_N$  value is used for both

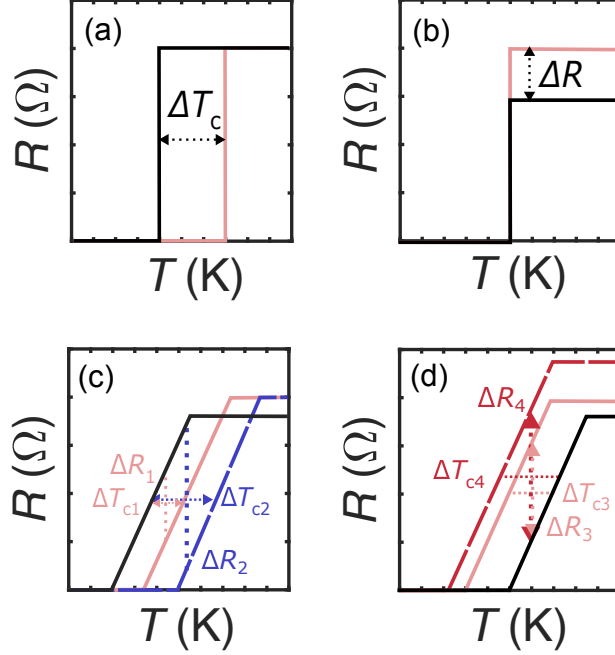


FIG. S3. Figures showing how the superconducting transition leads to a link between  $\Delta R$  and  $\Delta T_c$  values, exaggerated for clarity. (a) In an ideal device showing only the superconductor proximity effect, the parallel state (black) has lower  $T_c$  than the antiparallel (pink) state ( $\Delta T_c > 0$ ). (b) In an ideal device showing only GMR, the antiparallel state has a higher resistance above  $T_c$  than the parallel state ( $\Delta R > 0$ ). (c) A finite gradient in the superconducting transition links  $\Delta T_c$  and  $\Delta R$ . Here, for the same normal state  $\Delta R$ ,  $\Delta T_{c2} > \Delta T_{c1}$  ( $\Delta T_{c2}$  is more positive) causing  $\Delta R_2$  in the transition to be more negative than  $\Delta R_1$ . (d) Inversely, a larger  $\Delta R$  in the normal state can lead to a more negative  $\Delta T_c$ : here  $\Delta R_4 > \Delta R_3$ , so  $\Delta T_{c4}$  appears to have a greater (more negative) value than  $\Delta T_{c3}$ .

40 states as this gives a more representative value of the temperature instability allowed for a working device.

Temperature sweeps were performed at a rate of 0.3 K/min, using PID control. Higher cooling rates gave the same value of  $T_c$ , but this lower rate was used to ensure accuracy.  $R(T)$  sweeps from high to low temperatures are binned and averaged to minimise the effect of  
 45 random noise in  $R$ . The averaged parallel and antiparallel state curves are plotted together and the  $T_c$  value for each curve taken at  $0.5R_N$ , so that  $\Delta T_c = T_c^{AP} - T_c^P$  [Fig. S4(a)]. Temperature values are also taken at  $0.45R_N$  and  $0.55R_N$  which provide errors in each  $T_c$  measurement. The errors of each  $T_c$  are added in quadrature to give the error in  $\Delta T_c$ .  $T_{\text{device}}$

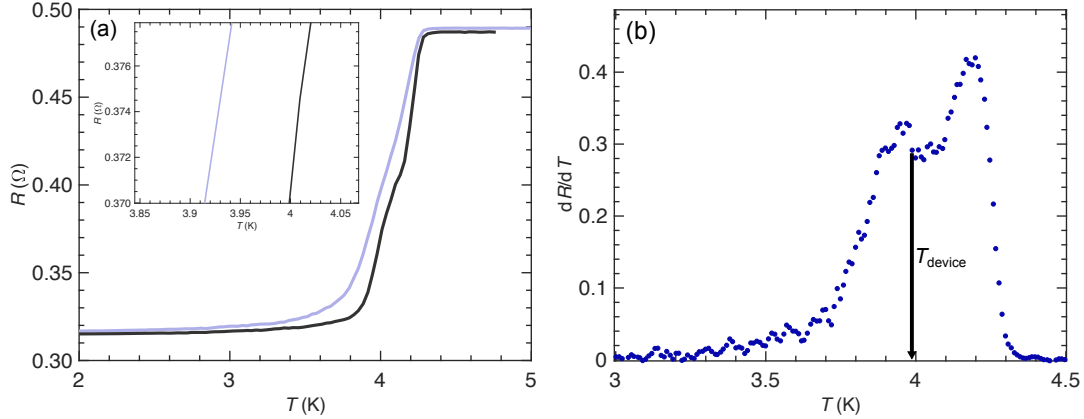


FIG. S4. (a)  $\Delta T_c$  is extracted from raw  $R(T)$  data in the parallel (black) and antiparallel (light blue) curves. The curves are zoomed in near  $R_N^{AP}$  (inset) and  $\Delta T_c$  is the difference between the temperatures corresponding to this resistance for each curve. (b)  $T_{\text{device}}$  is taken as the temperature at which the gradient of the antiparallel curve increases by 0.03 due to the device transition.

is the onset of the superconducting transition for the device. This is calculated from the  
 50 gradient of the antiparallel state  $R(T)$  curve, which is binned and smoothed by a moving  
 average.

$T_{\text{device}}$  is the temperature at which the gradient change associated with the device tran-  
 sition first exceeds 0.03 [Fig. S4(b)]. This value of 0.03 was chosen as a value exceeding  
 the basic noise level of the gradient data. Gradient is calculated from binned data and  
 55 smoothed by a moving median. Errors in  $T_{\text{device}}$  are the range of possible values that satisfy  
 this criterion.